PAPER • OPEN ACCESS

Insulated rail joint (IRJ) contact characterisation-an ultrasonic reflectometry approach for a cross-material interface

View the article online for updates and enhancements.

Insulated rail joint (IRJ) contact characterisation-an ultrasonic reflectometry approach for a cross-material interface

Lu Zhou[1], Yun-Ke Luo[2,3,*] and **Roger Lewis[1]**

[1] Department of Mechanical Engineering, The University of Sheffield, Sheffield, The United Kingdoms
[2] Hong Kong Branch of National Transit Electrification and Automation Engineering Technology Research Center, Hung Hom, Kowloon, Hong Kong Special Administrative Region of China
[3] Department of Civil and Environmental Engineering, The Hong Kong Polytechnic University, Hung Hom, Kowloon, Hong Kong Special Administrative Region of China

E-mail: yunke.luo@connect.polyu.hk

CrossMark

Abstract

Vehicle–track interaction at insulated rail joints (IRJs) plays a significant role in the wear evolvement and damage of the IRJ components. It is, however, challenging to characterise the contact conditions within the region non-destructively and accurately using experimental tools, especially when the IRJ contact involves both wheel–rail and wheel–endpost contact pairs. This study presents an ultrasonic technique to monitor and characterise static IRJ contacts in a non-invasive manner. The proposed ultrasonic reflectometry technique can realise high-resolution visualisation of contact patch and contact pressure distribution for both wheel–rail contact and wheel–endpost contact, by striking a beam of focused ultrasonic signals at the contact interface. Different data post-processing strategies are applied for the two types of contacts and a deconvolution algorithm is applied to rectify the measurements near the rail–endpost boundary. The ultrasonic measurements are verified through finite element simulations and the results show good agreement with each other in terms of both contact area and contact pressure level. It is expected that the proposed ultrasonic approach can be a reliable tool to assist in revealing the contact behaviour of IRJs more profoundly.

Keywords: structural health monitoring, wheel–rail contacts, insulated rail joints, ultrasonic reflectometry, cross-material interface

(Some figures may appear in colour only in the online journal)

1. Introduction

Insulated rail joints (IRJs) are critical components in railway systems interconnecting two adjacent rail sections as well as providing electrical isolation. Although in the era of high-speed rail, continuous welded rail is the primary option for safety and ride comfort purposes, IRJs are still necessary in freight lines and transition/low-speed zones in conventional lines. Railway lines are separated into individual sections by IRJs forming closed circuit loops (figure 1). When no train passes by the section, the signalling light within the circuit remains green; When a train enters the section, a short-circuit is created between train wheels and the power source, and the

---

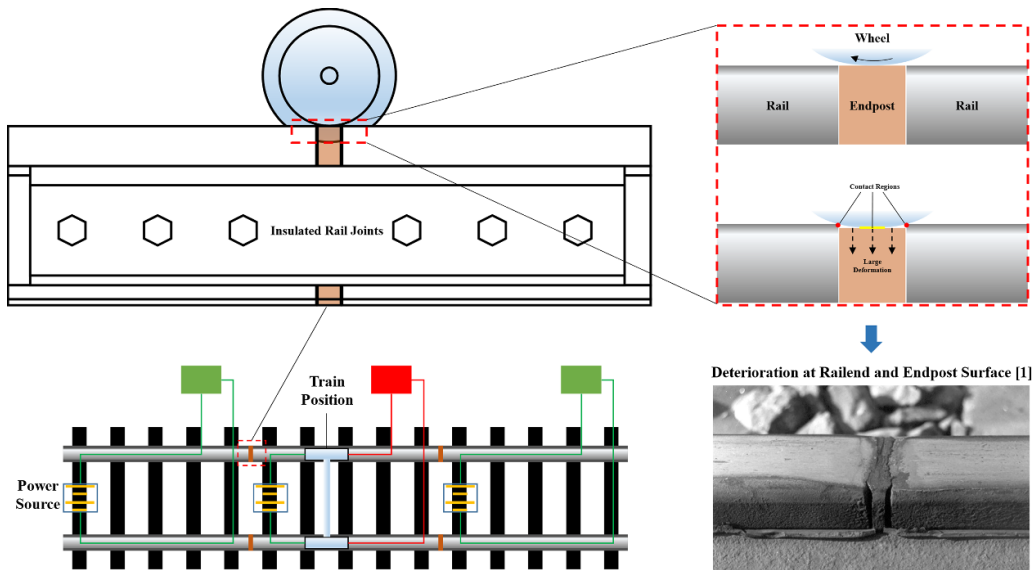* Author to whom any correspondence should be addressed.

Figure 1. Illustration of contacts and deterioration failure at IRJs.

signalling light turns red. In this way, the train location can be determined in real-time. To guarantee stable electrical isolation, the rail joint is bolted onto rail sections with an insulating layer inserted in between the components. Besides, a thin plate made of non-conducting composite materials (typically polymer, fibreglass, nylon, etc.), known as endpost is placed in the gap (4–10 mm wide) between two rail sections for insulation purpose. Since the endpost materials have a much lower elastic modulus and yield stress than rail steel, making the IRJs particularly vulnerable to damage and subsequent failure. As illustrated in figure 1, when a wheel passes over an IRJ zone, the endpost deforms in the normal direction, and the wheel load is mainly supported by the rail edges on each side, leading to extreme stress concentration and consequently causing spalling, shelling, or crushing at these spots. Moreover, under long-term intense wheel–rail impact and shear from traction in the contact, the rail edges suffer from plastic deformation in the longitudinal direction (lipping) and tend to squeeze and squash the endpost, resulting in deterioration and delamination [1]. Hence, understanding the mechanical behaviour of IRJs, especially the contact situation around the rail edge and endpost zone would be vital to precautious warning of failure and timely maintenance.

To investigate wheel–rail stresses around the IRJ zone, Chen conducted a series of finite element (FE) analyses concerning elastic and elastic–plastic contact under pure rolling or partial slip circumstances [1–3]. Sandström and Ekberg implemented an FE model for IRJs wheel–rail and wheel–endpost contact considering traction forces and compared the simulated contact stresses with Hertz predictions [4]. Mandal carried out systematic studies on ratcheting failure of IRJs subject to cyclic wheel loadings, with detailed contact stress distribution visualised through sub-modelling and FE simulations [5–8]. Numerical simulations have also been adopted by Yang *et al* to study the influence of wheel rail impact at IRJs [9–11].

Askarinejad *et al* conducted field experiments for structural assessment of IRJs through analysing response measurements under wheel–rail impact [12, 13]. Beaty *et al* established a model for lipping phenomenon at IRJs by twin-disc testing and offered a number of reinforcement suggestions [14]. Xiao *et al* utilised both field tests and 3D FE modelling to explore deformation of IRJs and estimate the wheel–rail impact force within the region [15].

Not surprisingly, almost all the literatures on IRJs contain a thorough investigation and presentation of wheel–rail contact, as it is the root cause of all types of failures in this area. Yet the tool to reveal specifically what is happening at the contact interface between wheel, rail and endpost is fairly limited, and numerical simulations or FE analysis seem to be the only way to visualise the contact stress distribution in detail. Either Hertz predictions [16] or Kalker's theory [17], or even the genuine profile 3D wheel–rail contact model developed by the authors recently [18] cannot handle contacts well that involve multiple bodies with different materials, since the wheel–endpost contact and wheel–rail contact has to be treated separately in these models and the structural information as an integrity is lost in the process. While FE is not always reliable in reflecting realistic situations, particularly in terms of surface roughness and wear conditions, and the approach is more suitable for validation rather than determination. In this regard, experimental ways to characterise the contacts within the IRJ region are highly desired, which is however not easy even for conventional wheel–rail contacts. Currently, in field tests, the wheel–rail contact force is mainly estimated indirectly by measuring the dynamic responses of rail tracks using an array of strain gauges or other sensors [19, 20]. Early attempts have been made to directly inspect the contact interface using airflow through pre-drilled holes on the rail head [21], or more recently, using pressure sensitive films [22, 23]. These methods can only provide vague contact pressure distributions, and

more importantly, the intruding sensing media inevitably alter the original contact situations, making the results less convincing. We are expecting a non-invasive measuring technique that can directly monitor the contact interface without changing the contact environment, which puts forward the utilisation of ultrasound for contact characterisation.

Applications of ultrasonic measuring techniques in railway systems have been widely seen covering active ultrasonic guided waves [24, 25], passive acoustic emission [26–28], phased array [29], air-coupled ultrasonic testing [30], and emerging ultrasonic structural health monitoring (SHM) techniques [31–33]. On the other hand, some recent research works linking ultrasonic sensing with contact mechanics can be found in [34, 35] by Song *et al* for bolt looseness monitoring based on fractal contact theory. To be more targeted to the task in the present study, a specific ultrasonic measuring technique, known as ultrasonic reflectometry, has long been utilised and investigated by the author for revealing contact conditions. The ultrasonic reflectometry enables contact characterisation by emitting a beam of ultrasonic signal which strikes at the contact interface and analysing the reflections. Roughly speaking, the more two contact bodies are pressed together, the lower the reflected ultrasound amplitude will be. By scanning over the entire area using a movable ultrasonic probe or an ultrasonic array, the contact patch can be visualised in a 2D manner. This technique has been used for determining contact pressure in bolted joints [36], ball bearings [37] as well as wheel–rail contacts under both static and dynamic circumstances [38, 39]. Transferring the existing approach for characterising contacts at IRJs appeared to be straightforward, but challenges emerged in the author's pilot study [40]. The key issue arises from the cross-material contact nature at IRJs and the ultrasonic probe scanning mechanism, in which the focus spot at the contact interface is not an infinitely small point but a circle with certain radius. When the focus circle passes over the boundary between rail steel and endpost composite, which have different acoustic properties, the measurement taken from this spot contains fused information from both wheel–rail and wheel–endpost contact zones, yielding inaccurate contact pressure results near the rail–endpost boundary. In face of issue, this paper presents a systematic study on contact characterisation at IRJs using ultrasonic reflectometry which enables high-resolution and reliable visualisation of contact pressure distribution at both rail edges and endpost areas. A specific data processing method is developed to disentangle the contact information within the focus circle and adjust the measurement near the boundary, concerning the energy distribution within the focus spot. A series of experiments are conducted under different wheel loads with different endpost thicknesses. 3D FE models are also developed in correspondence to the test specimens to compare with the results from ultrasonic experiments. Other than numerical approaches, this study offers a new way to characterise the contact at IRJs with reliable and informative details, which to the authors' best knowledge, is for the first of its kind measured in an experimental manner.

The rest of the paper is organised as follows: section 2 illustrates the principle of ultrasonic reflectometry as well as

the test design and setup for IRJ contact scanning; section 3 presents the data postprocessing from raw measurements to pressure distributions, including the developed boundary-close measurement adjustment method; section 4 displays the results after processing and comparisons with FE simulations, followed by detailed discussions. Section 5 lists the conclusions and future work.

2. Principles and test set-up

2.1. Ultrasound and interface

No matter how well a machine element is finished, the surface is not perfectly smooth at the microscale and is randomly distributed with asperities of various shapes. When two bodies are pressed together, it is the asperities that are in contact with trapped air gaps in between the contacts. When a beam of ultrasound strikes the contact interface, it will interact with the microporous structure, as shown in figure 2. If the wavelength of the incident ultrasonic waves is close to the air gap size, the ultrasound will be scattered at the interface; If the wavelength is considerably longer than the gap size, the ultrasound will be transmitted through the asperity contact regions and reflected at the air gaps. When increasing compression load is applied, more asperities are pressed into contact state causing higher transmission and less reflection. By measuring the reflection coefficient R, defined as the ratio of reflected acoustic energy by the incident acoustic energy (H_r/H_i), the contact state can be revealed.

Kendall & Tabor proposed a model for the ultrasound behaviours at the contact interface by treating the asperities as distributed compression springs [41]. In the *spring* model, the relationship between reflection coefficient R and the total equivalent stiffness of the springs, denoted as the interfacial stiffness K is determined as:

$$R = \frac{z_1 - z_2 + i\omega \left(z_1 z_2 / K\right)}{z_1 + z_2 + i\omega \left(z_1 z_2 / K\right)} \tag{1}$$

where z_1 and z_2 are the acoustic impedances of the two contact materials, defined as the product of material density and the speed of sound waves in the material ($z = \rho c$), ω is the angular frequency of the propagating ultrasound ($\omega = 2\pi f$). When there is no contact, K is zero as there is no asperity contact and R equals to one; under a theoretically extreme full contact state with no air gap, all ultrasonic energy is transmitted, K becomes infinity and R reaches the bottom limit (can be zero when the materials of two contact bodies are identical). Formal definition of the interfacial stiffness K is proposed by Thomas & Sayles [39] as the nominal contact pressure variation p_{nom} required to reduce the unit length of mean surface separation u between two contact bodies, written as:

$$K = -\frac{\mathrm{d}p_{nom}}{\mathrm{d}u}. \tag{2}$$

Although according to the definition, relationship between the interfacial stiffness and nominal contact pressure is well determined. While in real engineering contacts, the stiffness is
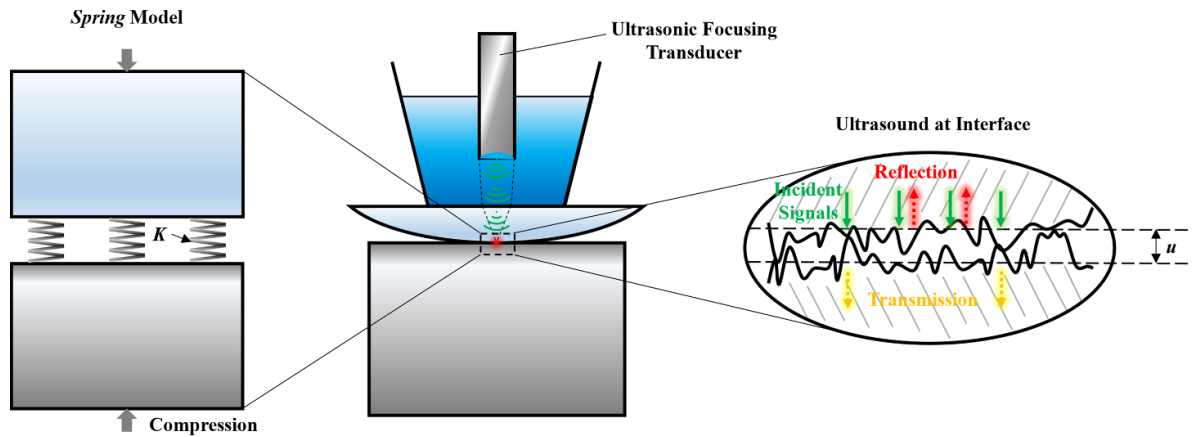
Figure 2. Ultrasound behaviours at contact interface and the *spring* model.

also dependent on the distribution, number as well as size of the asperity contacts [42]. Therefore, to obtain pressure distribution of a contact region, an additional test is required to obtain the K–P relationship for each unique surface roughness pair.

2.2. Test design and set-up

To characterise contact at the IRJ, an immersion ultrasonic focusing transducer was utilised. The transducer contains a piezo-electric plate that allows two-way alteration between electric energy and mechanical energy, i.e. it can generate an electric pulse subject to external deflection, and vice versa, therefore enabling both emitting and receiving ultrasonic signals. Since the transducer is specifically fabricated for immersion testing, distilled water was used as the couplant. As shear waves cannot propagate through a fluid couplant, the transducer only generates longitudinal waves. The emitted signal is expected to focus exactly on the contact interface of interest with proper water depth adjustment. The test specimens included a section cut from a full S1002 wheel, two 60 mm long UIC60 rail head sections and two nylon66 endpost head sections (profile same as the UIC60 rail) with thicknesses of 6 mm and 10 mm, as shown in figure 3. The rail sections and the endpost specimen were assembled with an external casing to constrain plane movement during the contact process under normal load. Material properties of the specimens are listed in table 1 (the wheel and rail steel are considered to be the same). The speed of sound in the propagating medium is determined by emitting a beam of ultrasonic signals to propagate a pre-measured distance in the medium and calculate the time-of-flight through the zero-crossing method, i.e. the time interval between two spots where the wave package of incident and reflected waves cross zero point for the first time.

A loading frame was used to clamp the test specimens, as shown in figure 4. The loading frame contains a pre-machined scanning window in the top plate to hold the distilled water couplant. Test specimens were placed in the loading frame with the wheel specimen on the top, and a wedge
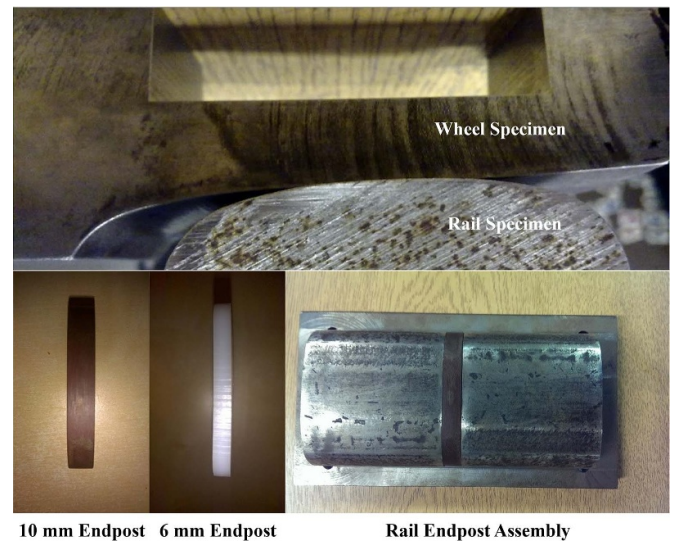

Figure 3. Pictures of test specimens.

Table 1. Material properties and model parameters.

Component	Parameter		Unit
Rail and wheel	Density	8190	kg·m^{-3}
	Speed of sound	5064	m·s^{-1}
	Young's modulus	210	GPa
	Poisson's ratio	0.3	—
Endpost	Density	1183	kg·m^{-3}
	Speed of sound	2600	m·s^{-1}
	Young's modulus	2.5	GPa
	Poisson's ratio	0.4	—

was inserted at the bottom of the specimens to guarantee perfect wheel tread-rail head contact, in alignment with the measures taken in operating railway systems. The load was applied to the specimens by a hydraulic pump to initiate contact. The loading frame was placed on a scanning tank which enabled two-directional plane movement driven by a step motor. The
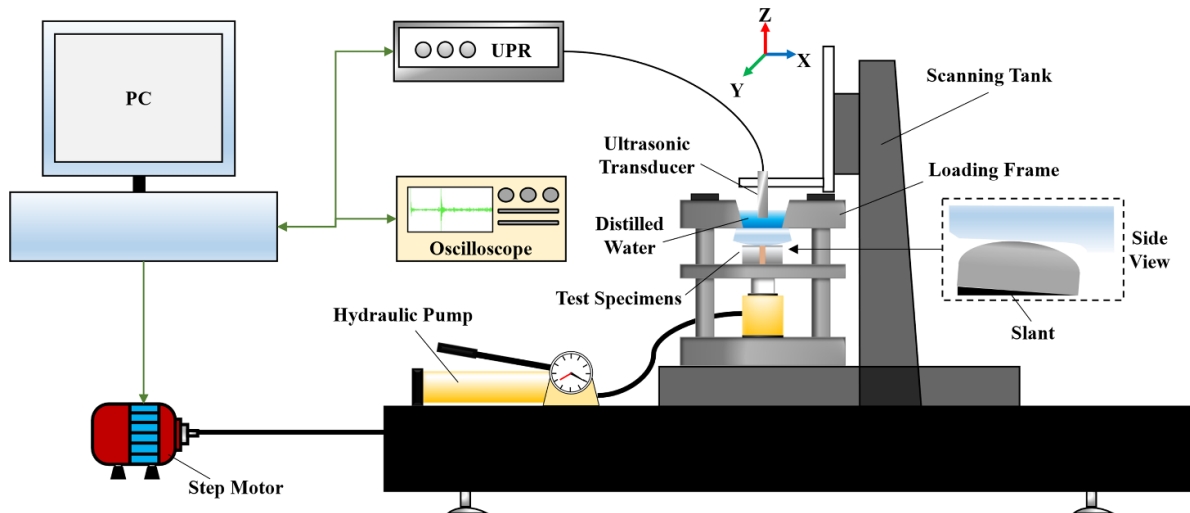
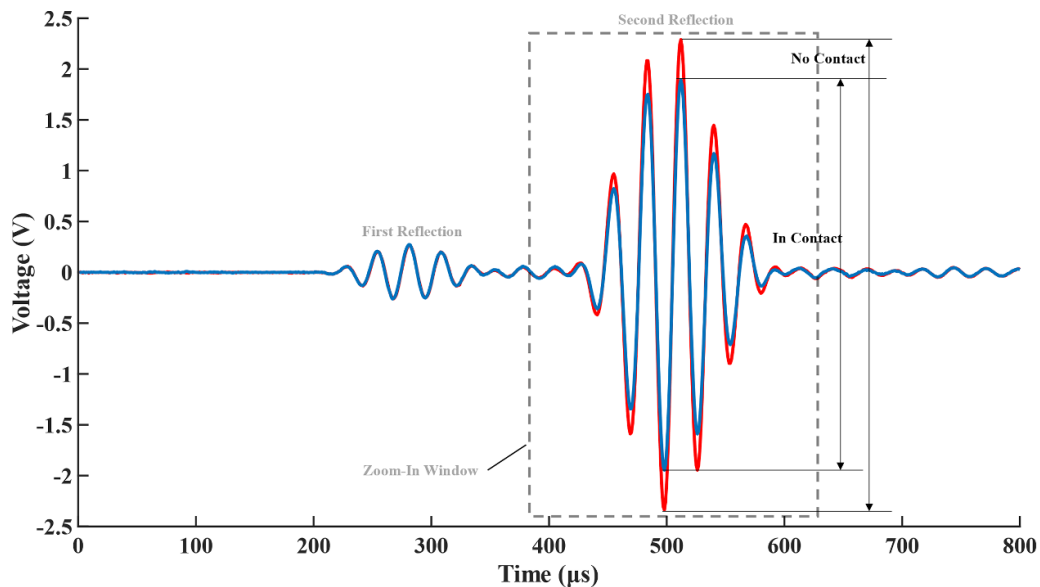**Figure 4.** Test setup for IRJ contact measurement.

Figure 5. A-scans of reflected waves and peak-to-peak value extraction.

focusing transducer was attached onto the scanning tank and immersed into water and the height was adjusted. An ultrasonic pulser and receiver device was connected to the transducer to generate and collect ultrasonic signals. A-scans of both incident and reflected waves were displayed through an oscilloscope.

Figure 5 illustrates example A-scans of the reflected waves, in which two reflections can be seen for each signal. The first reflection comes from the water–steel interface, but has a relatively small amplitude because the interface is not located in the focus plane. The second reflection is the wave package of interest from the wheel–rail and wheel–endpost contact interface. When the ultrasonic transducer scans over the contact area, the amplitude of the reflected voltage drops, and peak-to-peak values are extracted as the raw measurement. In

high contact pressure areas, the amplitude of the second reflection can be smaller than that of the first reflection. To make sure only the second reflection peak-to-peak values are collected, a filter window is applied. Since the wheel profile at the contact interface is curved, the position of the second reflection in the time domain experiences slight fluctuations in the scanning process, and the width of the filter window is set to be larger than that of the wave package.

The utilised transducer was a Spherical Focusing Immersion Transducer (Type IxHG Series A-style housing) purchased from NDT Systems Inc. with a frequency of 10 MHz which was a balanced option considering both precision and penetration distance. Lower frequency ultrasound is less sensitive in terms of sensing capability, while high frequency ultrasound suffers from more severe attenuation in the

Table 2. Ultrasonic transducer specifications.

Nominal frequency (MHz)	Focal length in water (mm)	Centre frequency (MHz)	Transducer diameter (mm)	Focused circle diameter (mm)
10	76	8.8	6.25	0.9

propagation process. Specifically, even at the focus plane, the ultrasound is focused to a finite circle. The diameter of the focus circle is determined by Krautkrämer and Krautkrämer [43] as:

$$\text{Spot diameter} (-6\,\text{dB}) = 1.025 \frac{l_\text{w} c_\text{w}}{f d_\text{c}} \tag{3}$$

where c_w refers to the sound speed in water, l_w is the focal length of the transducer in water, f is the ultrasound frequency, and d_c is the diameter of the piezo-electric crystal. Typically manufacturers produce ultrasonic transducers with known focal lengths in water, as in this medium the focal point can be calculated. Therefore, equation (3) is applicable only for focusing immersion transducer and the focal length used here is assuming the immersion transducer is only focusing in water. It should be noted that the nominal frequency of the transducer is 10 MHz, while in real applications it is difficult for a transducer to emit ultrasonic signal that sticks to a solitary frequency. The emitted waves contain a range of frequencies and the frequency containing maximum energy is the centre frequency, which in this study is 8.8 MHz. Specifications of the transducer are listed in table 2.

When in a test, the transducer moves in a zigzag way in the *x* and *y* direction and takes peak to peak values of reflected signals stepwise (as illustrated in figure 8 in the next section), eventually delivering a 2D plot of the scanned area. In this study, the ultrasound travelled through both water and wheel steel before reaching the contact interface, the ultrasonic waves got refracted at the water–steel interface, consequently shortening the focal length. As stated above, the height of the transducer to the wheel segment can be adjusted, and the transducer position in the normal direction was gradually adjusted to find the spot where the amplitude of the second reflection became largest, so that the focal spot was located exactly at the contact interface of interest. For the contact measurement test illustrated in figure 8, the wheel thickness at the scanning area is 20 mm, and the transducer is 43 mm above the top surface of the wheel specimen. But in whatever case, the focus spot diameter is a fixed specification for a certain type of transducer once fabricated. The scanning range was set to be 24 mm × 24 mm, and the step (resolution) is 0.1 mm. An example of the measured 2D voltage plot is shown in figure 6.

While from the voltage map, we may vaguely identify the contact patch already, but only in a qualitative manner. To achieve full contact pressure distribution, a series of data post-processing procedures need to be applied with details introduced in the following section.
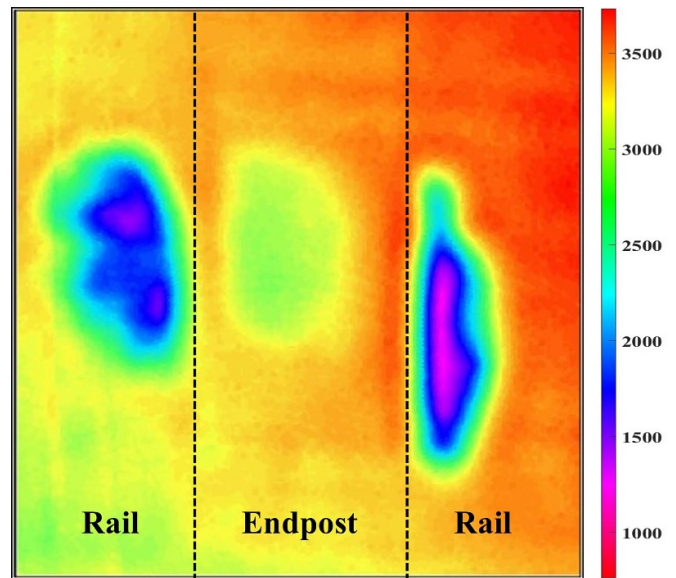

Figure 6. Voltage map (unit: mV) of IRJ contact measurement with 10 mm endpost under 60 kN load.

3. Data postprocessing

3.1. Reference measurement

Just as stated in section 2 that reflection coefficient is defined as the ratio between amplitude of the reflected ultrasound and that of the incident ultrasound, which is based on the presumption that the contact interface is uniformly perpendicular to the propagating direction of the incident wave. When the scanned profile at the interface is curved and not perfectly perpendicular to the propagation direction, as illustrated in figure 7, the waves will be scattered at the surface. To eliminate the influence caused by the curved profile, reference data is necessary, and R is calculated through the reflected voltage under a contact state divided by reference data. In the authors' previous work [37, 38], the reflected data can be one point, or one line of voltage data chosen from a non-contact region in the raw voltage measurements, since in these cases the rail head profile or the plate profile is either curved in one direction or flat. In this study, the scanning process can only be conducted through the wheel, which has curvature in both longitudinal and lateral directions. Therefore, an individual reference test had to be conducted by scanning the wheel profile without contact to generate a reference map, and the profile influence can be filtered out in the reflection coefficient.
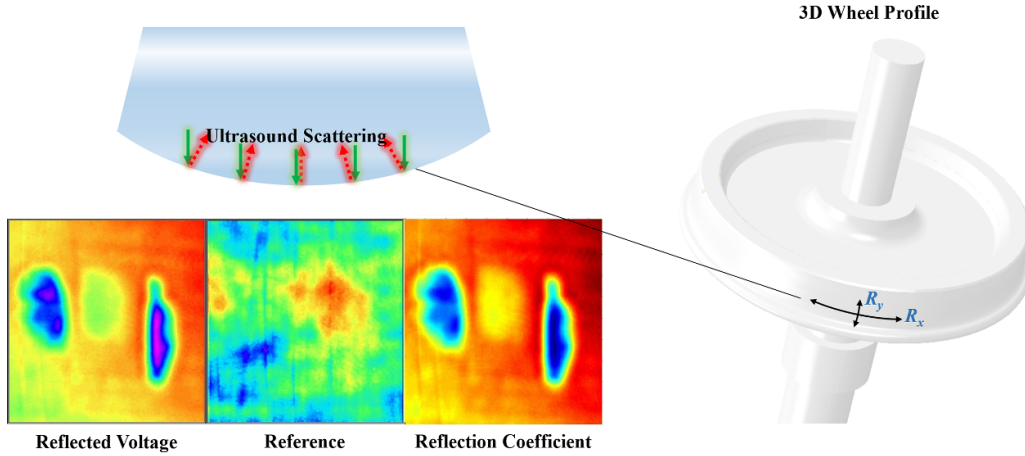
Figure 7. Ultrasound scattering at wheel profile and reference measurements.

3.2. Ultrasonic deconvolution

As listed in table 2, on the contact interface the emitted ultrasound has a circular focal spot with 0.9 mm diameter, which means each measurement is taken as a weighted average within the focus circle. In other words, it is the convolution product of ultrasonic energy distribution and real values in the circle A_{focus}, as demonstrated in equation (4):

$$V_{\mathrm{m}} = \iint\limits_{A_{\mathrm{focus}}} E_{\mathrm{norm}}(x, y) V(x, y) \, \mathrm{d}S \tag{4}$$

where V_{m} is the measured voltage value, $E_{\mathrm{norm}}(x, y)$ is the normalised acoustic energy distribution in the focus circle, and $V(x, y)$ refers to the real reflected voltage distribution. Since the reference voltage matrix is contact-independent, equation (4) can be transformed to the reflection coefficient perspective:

$$R_m = \iint\limits_{A_{\mathrm{focus}}} E_{\mathrm{norm}}(x, y) R(x, y) \, \mathrm{d}S. \tag{5}$$

When the ultrasonic probe moves at a 0.1 mm step delivering a 240×240 resolution map in the 24 mm $\times$ 24 mm scanning window, the map is a matrix of convoluted values, and neighbouring pixels have major overlapping areas. For characterisation of conventional machine element contacts which do not involve cross-material contact, it is acceptable to use the convoluted measurements as an estimation of the real values. As for this study, however, this is not accurate at the rail–endpost boundary. As illustrated in figure 8, when the focus circle passes over the boundary line, the convolution contains both low reflection (high contact pressure) information in the wheel–rail contact region and high reflection (low contact pressure) information in the wheel–endpost contact region, which significantly alters the contact pressure results. Hence, a deconvolution process needs to be conducted considering the ultrasonic energy distribution to reveal the real values at the focus centre.

As investigated by Krautkrämer *et al* [43], for spherical focusing transducers, the radial acoustic pressure at the focus plane can be calculated as:

$$P = p_{\max} abs \left(\frac{2J_1(X)}{X} \right) \text{ where } X = \frac{\pi D q}{\lambda z_{\mathrm{f}}}. \tag{6}$$

$p_{\max}$ is the peak acoustic pressure at the focal point, z_{f} the focal length (in water), λ the ultrasonic wavelength (in water), D the diameter of the transducer, q the radial distance from the transducer centre line, and J_1 the Bessel function of the first kind. The focus spot is a circle, for a 2D sound pressure distribution, $q = \sqrt{x^2 + y^2}$. Substituting the specifications of the transducer used in this study, the radial and 2D sound pressure distribution can be plotted, as shown in figure 9. Noting that equation 6 has a discontinuity of the first kind at $q = 0$ point which can be removed by defining $P(0) = \lim\limits_{q=0} P(q)$.

It can be seen from figure 9 that the focus circle covers the primary lobe and approximately a quarter of the secondary lobe. Therefore, equation (5) can be transformed into the following form:

$$R_m = \int\limits_{-0.45}^{0.45} \int\limits_{-\sqrt{0.9^2 - x^2}}^{\sqrt{0.9^2 - x^2}} p'_{\max} abs$$

$$\times \left(\frac{2J_1\left(\pi D \sqrt{x^2 + y^2} / (\lambda z_{\mathrm{f}})\right)}{\pi D \sqrt{x^2 + y^2} / (\lambda z_{\mathrm{f}})} \right) R_{\mathrm{dec}} \mathrm{d}x \mathrm{d}y \tag{7}$$

where $p'_{\max} = \left(\int\limits_{-0.45}^{0.45} \int\limits_{-\sqrt{0.9^2 - x^2}}^{\sqrt{0.9^2 - x^2}} abs \left(\frac{2J_1\left(\pi D \sqrt{x^2 + y^2} / (\lambda z_{\mathrm{f}})\right)}{\pi D \sqrt{x^2 + y^2} / (\lambda z_{\mathrm{f}})} \right) \mathrm{d}x \mathrm{d}y \right)^{-1}$

is the normalised peak pressure value to generate a probability distribution function $E_{\mathrm{norm}}(x, y)$, or more generally denoted as the point spread function (PSF) within the focus circle in imaging deblurring. Although the PSF is pre-known nominally, the actual PSF can be different subject to manufacturing variance and other uncertainties. Conventional deblurring algorithms such as Wiener filter do not exhibit good performance, and blind deconvolution which is widely adopted
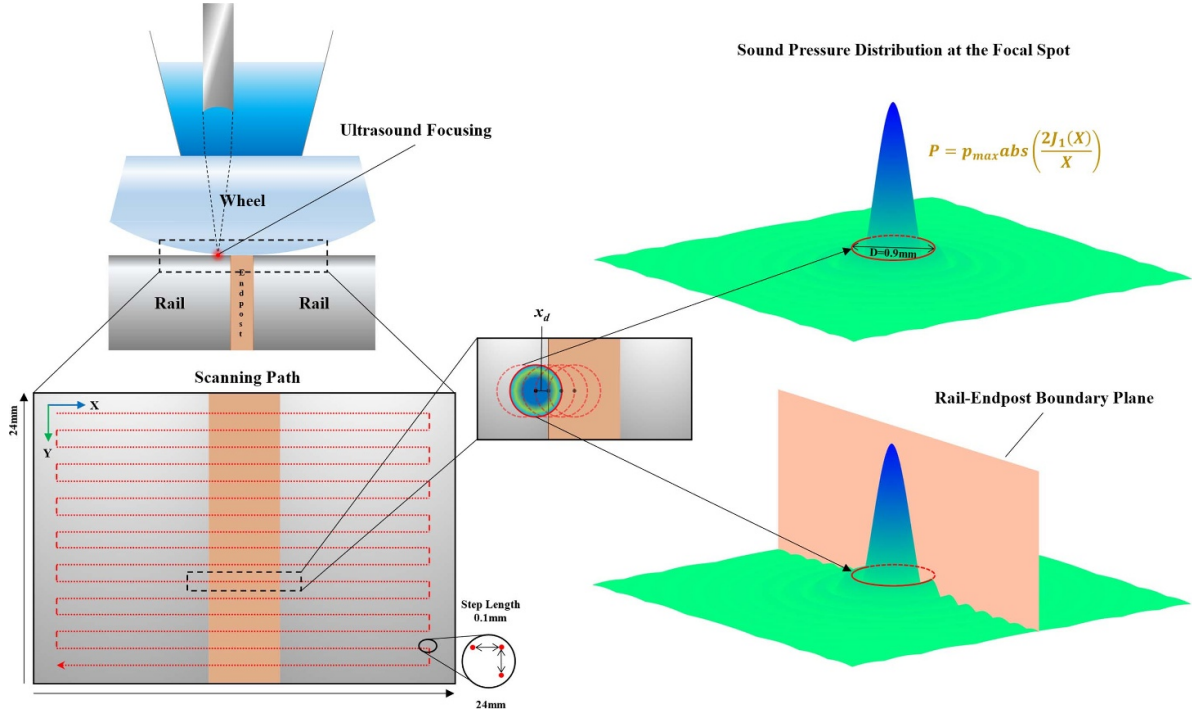
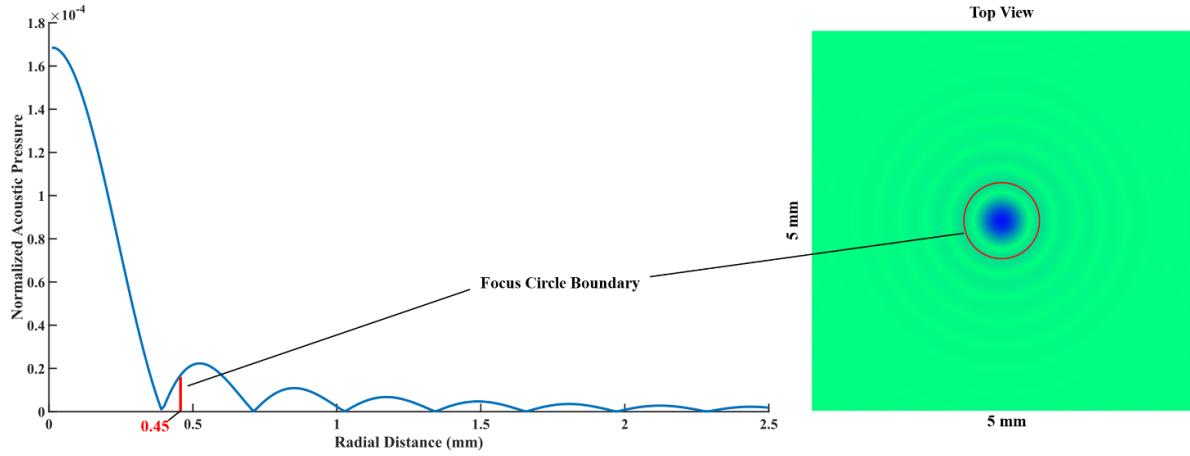**Figure 8.** Ultrasonic convolution at rail–endpost boundary.

Figure 9. Radial and 2D sound pressure distribution for the 10 MHz transducer.

in ultrasonic imaging over the past decades [44–46] is more appropriate in this study. The blind deconvolution algorithm used in this study is based on maximum likelihood estimation, and the nominal PSF serves as the initial PSF which is updated through iterations. Eventually, the recovered 240 * 240 reflection coefficient matrix R_{dec} can be obtained from the 240 * 240 measured matrix R_m through the discrete blind deconvolution.

Recall that R in equation (1) can be complex value, what is obtained from the measurements is the modulus of R, denoted as $|R|$. By taking modulus of both sides, the interfacial stiffness can be derived from:

$$K = \omega z_1 z_2 \sqrt{\frac{1 - |R|^2}{|R|^2 (z_2 + z_1)^2 - (z_2 - z_1)^2}}. \tag{8}$$

To guarantee K is a real number, $|R|$ has top limit '1' and bottom limit $|(z_2 - z_1)/(z_2 + z_1)|$. In practical test, real $|R|$ measurements experience fluctuations and can go beyond the top or bottom limit subject to electrical interference, environmental noise, or marginal effect between two adjacent ultrasonic pulses, etc. These values were replaced with interpolations from neighbouring measurements after deconvolution. It is worth mentioning that in terms of wheel–rail contact part
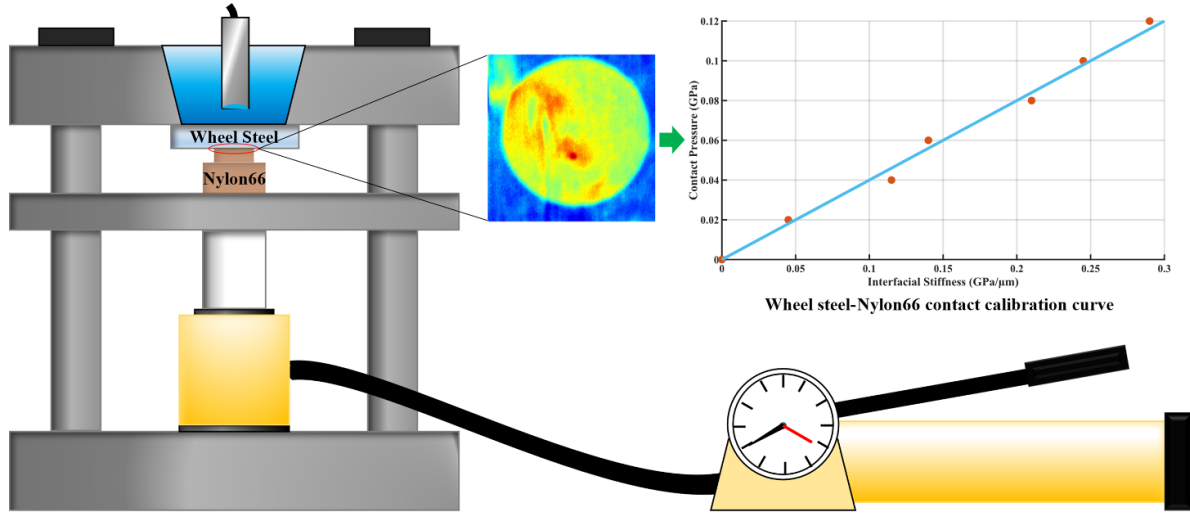
Figure 10. *K–P* calibration test for steel-Nylon66 contact.

where $z_1 = z_2 = z$, the theoretical bottom limit is zero, and the interfacial stiffness can be calculated from:

$$K = \frac{\omega z}{2} \sqrt{\frac{1}{|R|^2} - 1}. \tag{9}$$

3.3. Calibration test

As mentioned in section 2 the interfacial stiffness K is not only dependent on the contact pressure P but also on the asperity distribution, number, and size, which is manifested at the macro scale as 'surface roughness'. Therefore, the $K–P$ relationship is different under different surface roughness. In terms of the wheel–rail contact situation, Marshall *et al* [47] investigated the $K–P$ relationship under different wheel–rail surface roughness pairs through a series of calibration tests. For this study, $P = 0.418^*K$ for the wheel–rail contact part. In terms of wheel–endpost contact, a separate calibration test is needed.

The calibration test was carried out by measuring contacts between a wheel steel plate and a 3 mm radius Nylon66 cylinder which created a $r = 3$ mm circular contact patch. The steel plate and nylon cylinder were cut from wheel and endpost specimens identical to the ones in normal tests in terms of surface roughness. Reflected voltage measurements were taken under load series from 10 kN to 60 kN at a 10 kN step, and the interfacial stiffness map can be derived subsequently. The pressure is regarded as evenly distributed within the contact patch in calibration test and is calculated by dividing the load with nominal contact patch, i.e. πr^2. A scattering plot can be drawn from the six calibration results together with the (0, 0) point when there is no contact. Linear fitting the scattering plot delivers the $K–P$ relationship for steel-nylon66 contact tested in this study, as shown in figure 10. For the calibration test, the wheel steel plate thickness at the scanning area is 10 mm,

and the transducer is 60 mm above the top surface of the steel plate.

Consequently, the $K–P$ relationship is determined as $P = 0.4^*K$. Up to this step with all the data postprocessing procedures included, finally, the contact pressure distribution can be inferred. For demonstration clear purpose, a summary of the procedures can be referred from figure 11.

4. Results and validation

4.1. Contact pressure scanning results

Following the procedures illustrated in section 3, we can obtain 2D pressure maps of IRJ contacts under all loads for both 6 mm (figure 12) and 10 mm (figure 13) endpost cases. To clearly view the contact patch and pressure variation, contour plots are used for demonstration, and a non-isometric legend is added so that pressure of both wheel–rail contacts and wheel–endpost contacts can be visualised in detail. It can be instantly viewed from the pressure maps that most of the applied load is supported at the two rail edges, and the contact pressure on the endpost remains at a low level as expected. In terms of the contact patch, since it is hard to apply load exactly at the centre line of the test specimens during the loading process, the load supported at two rail edges is to some extent different, and such asymmetry is also manifested by the measured contact patches on two sides, the size of which grow steadily with the increasing load. The contact patches at the endposts (both 6 mm and 10 mm) appear as irregular strips/rectangles. They do not appear to grow as load increases. Unlike Von-mises stress distribution at two rail sections as simulated in previous FE works [5, 6], it is found that the peak contact pressure areas do not locate precisely at the rail edge on both sides, but with a certain offset. This is attributed to deformation (primarily in the elastic form) of the rail edges under high contact pressure, creating chamfer-like areas
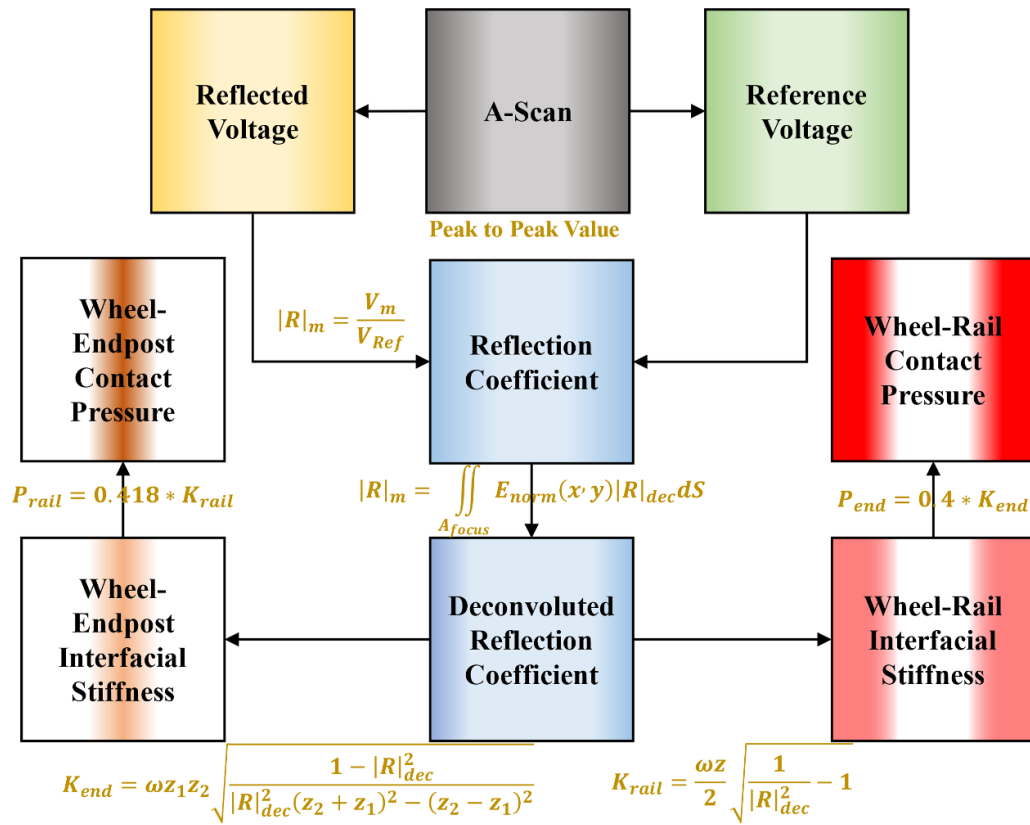
Figure 11. Data post-processing flowchart.

$$|R|_m = \frac{V_m}{V_{Ref}}$$

$$|R|_m = \iint_{A_{focus}} E_{norm}(x, y)|R|_{dec}\, dS$$

$$P_{rail} = 0.418 * K_{rail}$$

$$P_{end} = 0.4 * K_{end}$$

$$K_{end} = \omega z_1 z_2 \sqrt{\frac{1 - |R|_{dec}^2}{|R|_{dec}^2 (z_2 + z_1)^2 - (z_2 - z_1)^2}}$$

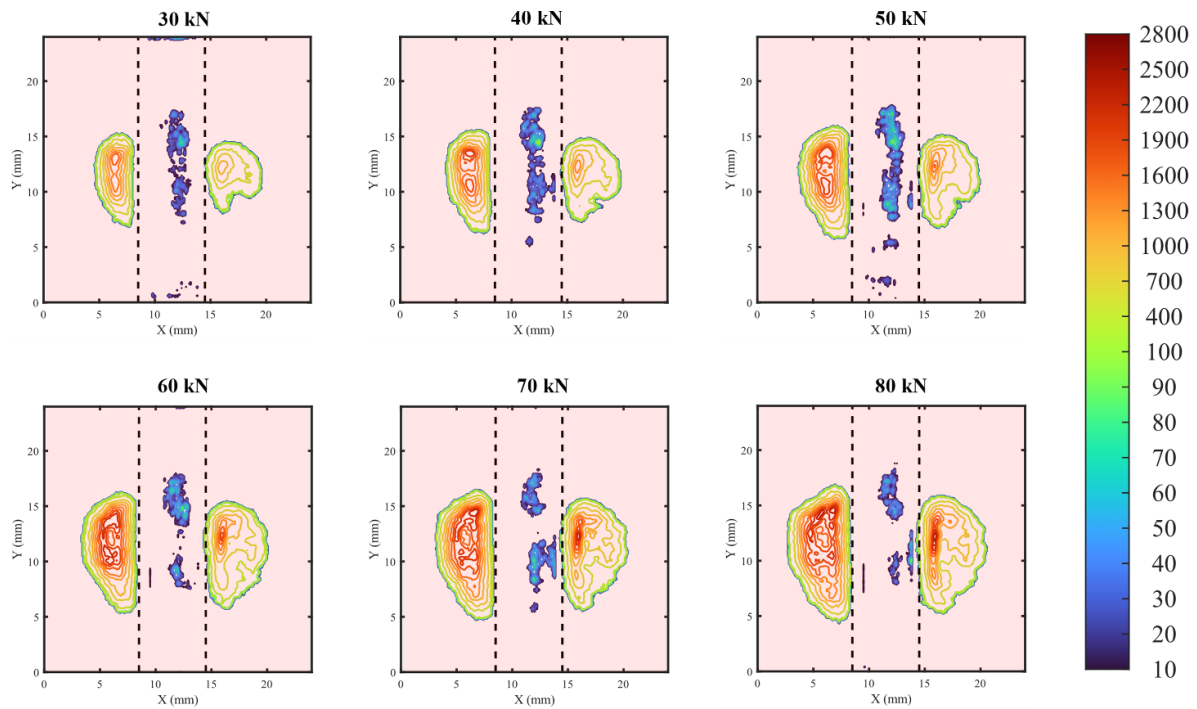$$K_{rail} = \frac{\omega z}{2} \sqrt{\frac{1}{|R|_{dec}^2} - 1}$$

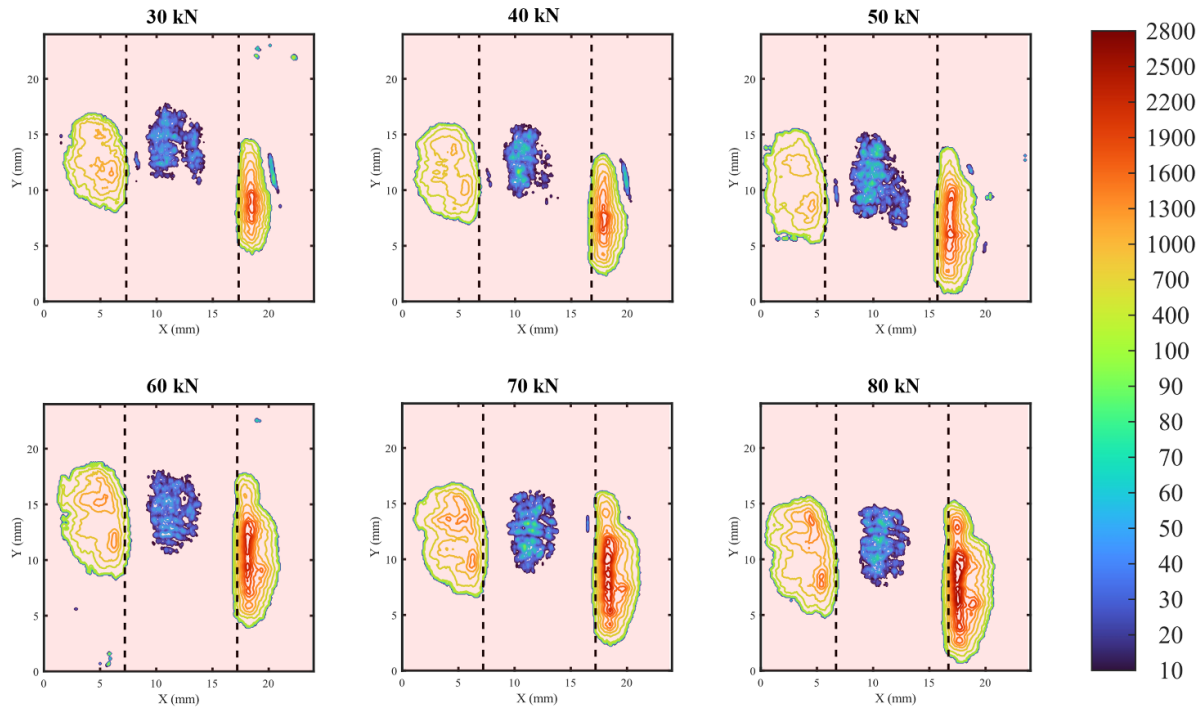**Figure 12.** Measurements with 6 mm endpost (MPa).

Figure 13. Measurements with 10 mm endpost (MPa).

at the sharp corners. While it is worth noting that deformation of the areas that are nearly in contact (close-contact areas) also causes an amplitude drop of ultrasonic reflections, the recognised contact areas from ultrasonic measurements are normally larger than the real nominal contact areas. In this case, a threshold is applied to the reflection coefficient map as a contact state indicator for wheel–rail contacts, i.e. a reflection coefficient above the threshold (or equivalently the pressure below a limit under each load) is recognised as 'non-contact'. Here we follow the same strategy as our previous work [39] upon a series of validation experiments by choosing the reflection coefficient threshold as 0.9 which is generally sufficient for normal wheel–rail contact, but for rail edges with larger deformation, the threshold may mis-recognise some close-contact region as a 'contact' state. Therefore, it can be noticed that a small portion of the wheel–rail contact patch surpasses the rail–endpost boundary in some cases because of this. Nevertheless, this is mainly a matter of threshold selection and does not substantially influence the overall results and discussions.

4.2. FE simulations

For comparison and validation purposes, a 3D model of the test specimens was established and meshed in Abaqus with properties listed in table 1. Balancing both simulation resolution and computing efficiency, the global mesh size for the wheel–rail–endpost FE model was defined as 3 mm. The mesh in the potential contact regions was refined, with a mesh size of potential wheel–rail contact area of 0.5 mm and that of potential wheel–endpost contact area as 0.25 mm. A directional sweep mesh algorithm was chosen to conduct the element

size transition from the densely meshed areas to non-contact regions. A hex-dominant meshing strategy was adopted, and the element types were C3D6 and C3D8R. Normally the master surface of a surface-to-surface contact definition should hold a finer mesh condition, hence the rail and endpost surfaces were defined as the master surfaces, and the wheel surface was defined as the target surface. The rail–endpost side contact and wheel–rail–endpost contact were defined as frictional with a friction coefficient of 0.25 according to relevant measurements [48, 49]. The total element number was 277 098 for the model with a 6 mm endpost and 291 808 for the model with a 10 mm endpost (figure 14).

The model was solved by the quasi-static implicit solver. This algorithm holds the best convergence behaviour because of the introduced inertia effects for regularising unstable behaviours. The general static analysis algorithm, which is based on Newton's method, has a finite radius of convergence, and was thus discarded in our highly nonlinear, large element matrix size and discontinuity solution procedures.

In alignment with ultrasonic tests, load series from 30 kN to 80 kN with a 10 kN step was applied for both 6 mm and 10 mm endpost cases. An example (10 mm endpost, 80 kN) of deformation in the normal direction of rail sections and endpost within the contact regions is shown in figure 15. Not surprisingly the endpost deforms significantly more than the rail edges (around 0.12 mm against 0.07 mm), which is why the rail sections support most of the load.

Contact patches on both rail edges and endpost grow steadily in correspondence to the increasing load, which can be applied precisely along the centre line of the endpost in FE simulations, delivering a more symmetrical pattern. It is noticed in FE simulations that a minor portion of the
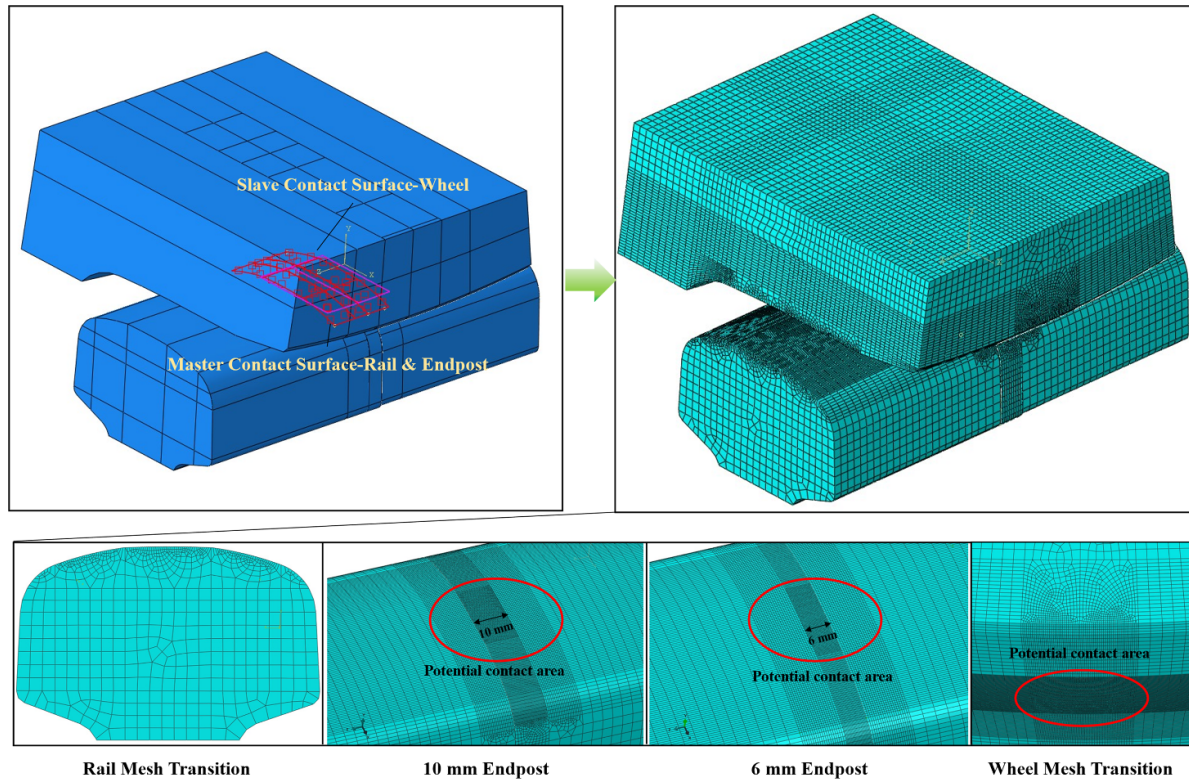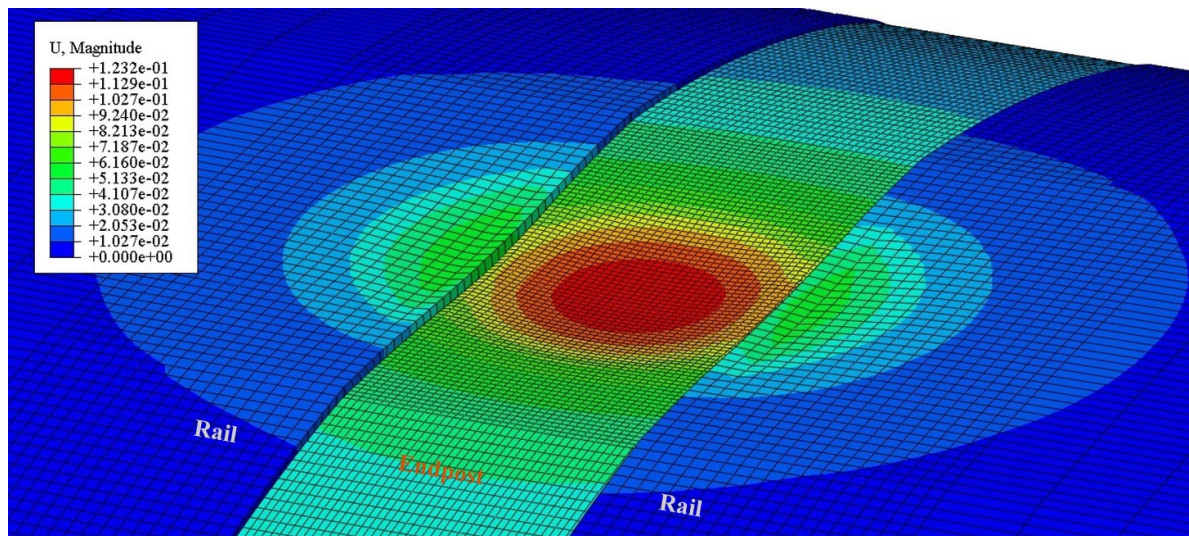
Figure 14. Wheel–rail–endpost FE model.

Figure 15. Deformation of rail and 10 mm endpost under 80 kN (unit: mm).

wheel–rail contacts also surpasses the rail–endpost boundary. This is mainly ascribed to the limit of mesh size, in which transition is unavoidable for solutions of two adjacent elements. The same as ultrasonic measurements, while we are keener on the contact pressure on the rail edges, these regions are neglectable and can literally be treated as non-contact regions. Further comparisons and discussions are presented in the next subsection.

To enable more straightforward comparison between FE simulation results and ultrasonic measurements, simulation results are exported as separate data files and imported into MATLAB to generate contour maps of contact pressure, as illustrated in figures 16 and 17.

4.3. Result comparison

Areas of wheel–rail contact (summation of rail edges on two sides) and wheel–endpost contact from FE simulations and ultrasonic measurements are tabulated in table 3, the area of wheel–endpost contact is in the brackets.
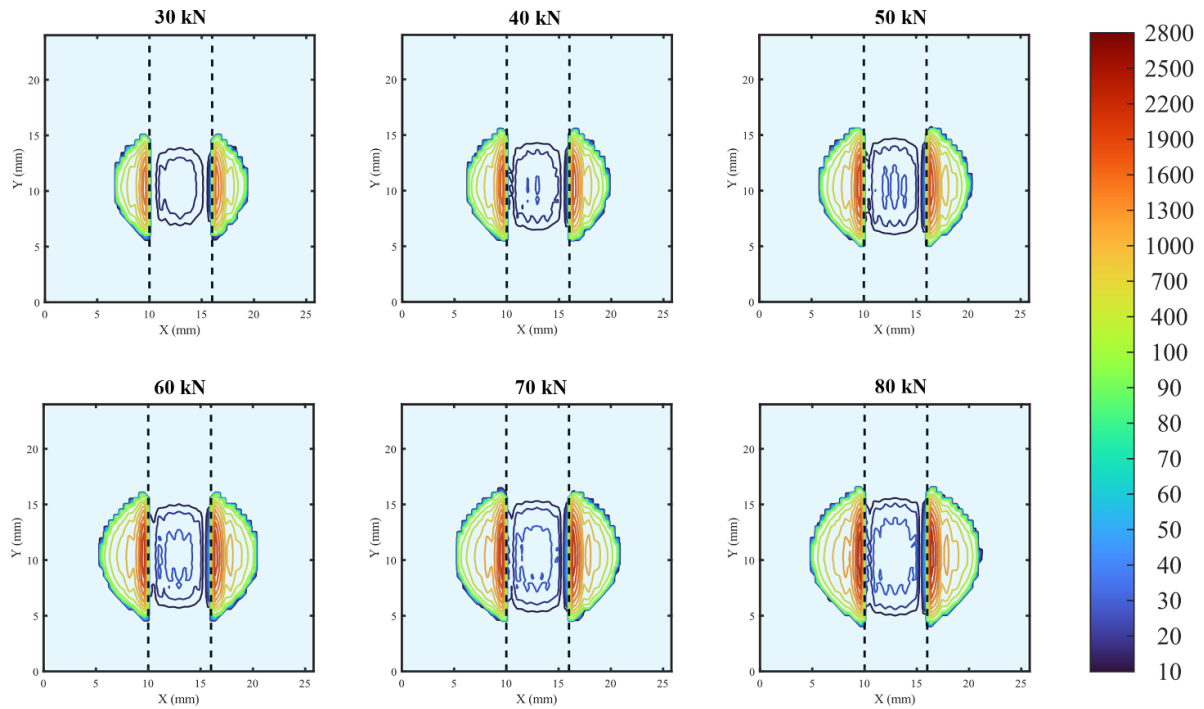
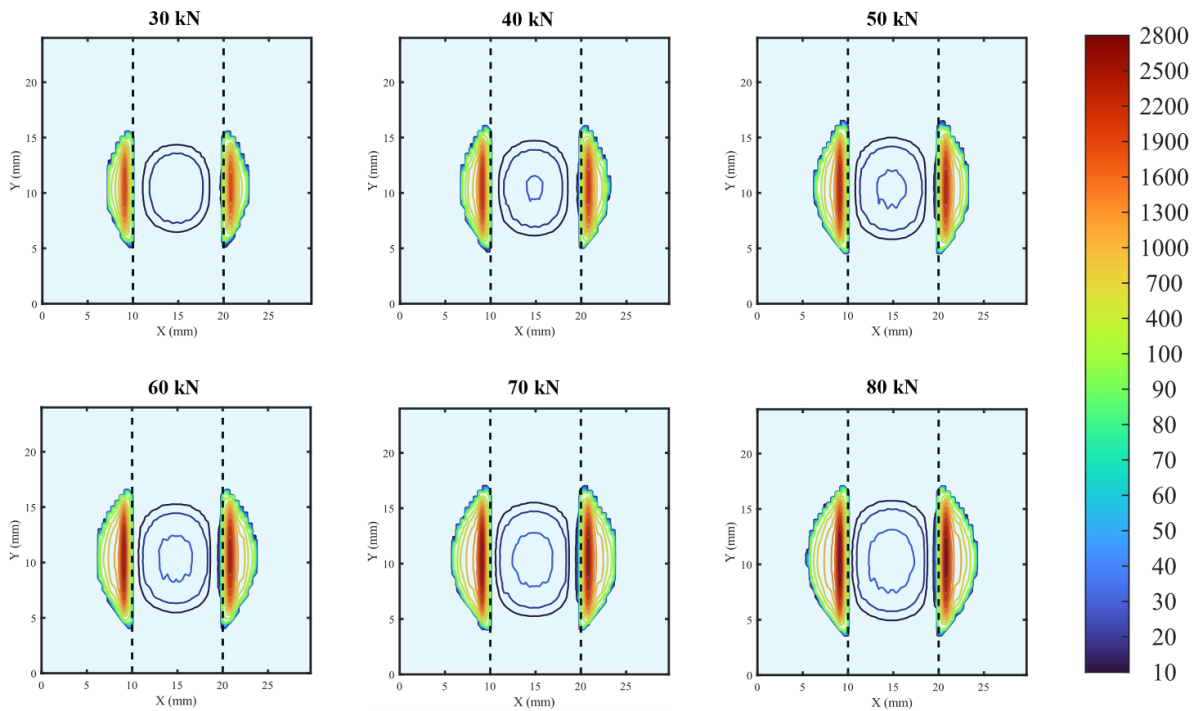**Figure 16.** Simulated contact pressure with 6 mm endpost (MPa).

Figure 17. Simulated contact pressure with 10 mm endpost (MPa).

Although the contact patches in FE simulations are more regular than ultrasonic measurements, the total contact areas at rail edges are in good agreement between two approaches for both 6 mm and 10 mm cases. As with the endpost, contact area from FE simulation results has a subtle linear growing trend from 30 kN to 80 kN, while that from ultrasonic measurements does not exhibit any obvious correlation with the

load and remains at a relatively low level which is much smaller than FE results. Moreover, non-contact gaps are observed for almost all cases (including FE simulations for 6 mm case although barely visible due to mesh size limitation). Based on these, a natural presumption can be made that wheel–endpost contact does not develop any further once the load goes beyond a certain threshold, which is smaller than 30 kN, and contact

Table 3. Contact area of wheel–rail contact and wheel–endpost contact (unit: mm^2).

	6 mm-endpost case		10 mm-endpost case	
	Contact area of wheel–rail contact and (wheel–endpost contact)			
Load	FE model	Measurement	FE model	Measurement
30 kN	55 (32)	44 (10)	45 (64)	61 (19)
40 kN	65 (35)	57 (13)	54 (70)	68 (15)
50 kN	77 (38)	67 (15)	62 (76)	83 (25)
60 kN	86 (42)	80 (10)	70 (81)	92 (21)
70 kN	96 (44)	89 (11)	78 (86)	91 (20)
80 kN	105 (47)	100 (8)	85 (90)	100 (21)

Table 4. Peak pressure of wheel–rail contact and wheel–endpost contact (MPa).

	6 mm endpost case		10 mm endpost case	
	Peak pressure of wheel–rail contact and (wheel–endpost contact)			
Load	FE model	Measurement	FE model	Measurement
30 kN	1520 (23)	1490 (75)	1780 (25)	2100 (66)
40 kN	1680 (25)	1840 (112)	1970 (28)	2150 (100)
50 kN	1811 (28)	1870 (94)	2130 (30)	2200 (89)
60 kN	1930 (31)	1950 (87)	2260 (32)	2470 (58)
70 kN	2030 (33)	2070 (84)	2380 (34)	2640 (97)
80 kN	2130 (35)	2160 (92)	2500 (35)	2830 (81)

development is basically manifested on wheel–rail contact regions. The subtle increment in wheel–endpost contact size from FE simulations is mainly due to the underlying computing algorithm of the contact solver that binds load with pressure, and such change does not make any remarkable contribution to the overall state within the IRJ contact region.

To further verify our presumption, peak contact pressures of wheel–rail contact and wheel–endpost contact from two approaches are listed in table 4 in the same way.

The general contact pressure level from either FE simulations or ultrasonic measurements is distinctly larger than normal wheel tread-rail head contact, as revealed in [38, 43] (where the maximum contact pressure was determined as 1400 MPa under 80 kN), indicating a much harsher contact condition in the IRJ region.

For wheel–rail contact at rail edges, concerning the 6 mm endpost case, the peak pressures from ultrasonic measurements match well with FE simulation results but are a little higher. This is because surface roughness which leads to surface irregularities is not included in FE model, and the stress concentration areas induced by surface irregularities cannot be simulated, but these features can be captured through ultrasonic scanning over real surfaces of test specimens. As with the 10 mm endpost case, the pressure difference between ultrasonic measurements and FE simulations goes larger (from approximately 2% to 10%), because a more severe asymmetrical loading condition is experienced in the 10 mm endpost test, which can also be clearly viewed through the contact patches in figure 13. Despite this, the agreement is generally satisfactory. It is also noticed that peak pressures of the 10 mm endpost case under all loads are higher than those of the 6 mm

endpost case for both ultrasonic measurements and FE simulations, indicating that even neglecting the asymmetrical loading bias, rail edges with 10 mm endpost suffer from higher wear or damage risk under a more intense contact environment.

When it comes to peak pressure on the endposts, a similar trend is observed to what is found on contact size variation, that FE simulations deliver mild and linear increasing results from 25 MPa to 35 MPa while ultrasonic measurements are not influenced by the increasing load but fluctuate within the 50–100 MPa range, and the outlier peak pressure that goes beyond the range is more likely caused by the surface irregularities (corrugation) on the endpost. For both FE simulations and ultrasonic measurements, while the contact area on the 10 mm endpost is doubled over the 6 mm endpost, pressure level of the two is approximately the same.

Based on the comparisons and deformation within the IRJ contact region, we may complement our presumption on the contact behaviour of IRJ under wheel loading: when a train passes by the IRJ region, the endpost sustains up to 100 MPa contact pressure and deforms significantly. The deformation along the longitudinal direction is not a fixed value, but exhibits a concave shape, which however does not indicate the wheel–endpost contact is conformal. Edges of the endpost are in the out-of-contact state, leaving gaps within the area. The rail edges on two sides support most of the normal load with contact pressure much higher than normal wheel tread-rail head contact and deform to the state of a chamfer- or slope-like area, hence the maximum contact pressure does not locate exactly on the rail–endpost boundary as one may anticipate, but 0.5 mm-1 mm away. In the long-term in-service situation, the rail sections have a tendency 'flowing' towards
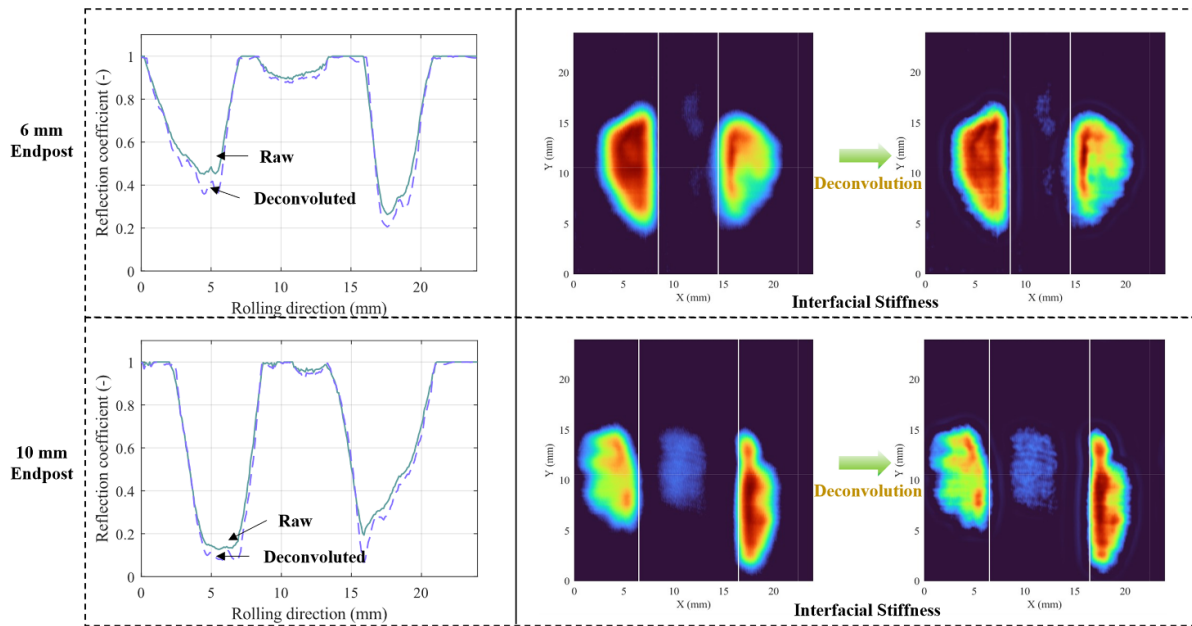
Figure 18. Demonstration of example reflection coefficient line and interfacial stiffness map before and after deconvolution.

the endpost and squashing the component, deteriorating the rail surfaces meanwhile speeding up the failure process of the endpost.

4.4. Deconvolution demonstration

Post to the main content on contact analysis and discussions, it would also be interesting to demonstrate how deconvolution rectifies the ultrasonic scanning results. As stated in section 3, the blind deconvolution result based on maximum likelihood estimation is strongly influenced by the initial condition of PSF including distribution function and range. In the present work, a normalized 10×10 initial PSF matrix based on equation (6) was generated, and its element size was defined as 0.1 mm, which is consistent with the transducer specification and scanning step. An example showing a line of reflection coefficient before and after deconvolution within IRJ contact region with both 6 mm and 10 mm endpost under 80 kN load is demonstrated in figure 18, together with the corresponding maps of interfacial stiffness. An apparent drop can be observed on the reflection coefficient after the deconvolution at two rail edges close to the rail–endpost boundary, implying considerably higher pressure than raw measurements and therefore presents results comparable with FE simulations. Moreover, the deconvoluted interfacial stiffness maps also evidently reveal more details within the entire IRJ contact region. We tried replacing the prior knowledge of initial PSF derived from equation (6) with a standard 2D Gaussian distribution but received completely incorrect results with distorted contact patches, confirming the importance of knowing nominal PSF of the transducer in data post-process. Poor performance was also found when applying non-blind deconvolution algorithms. Systematically exploring the sensitivity of deconvolution is meaningful but goes beyond the main topic of this study and is therefore not presented here.

5. Conclusions

Experimentally monitoring wheel–rail contacts is never an easy task, and characterising contacts at IRJs with cross-material interface can be even more challenging. As an advancement of the author's previous research in this area, this study presents a contact characterisation method at IRJs using ultrasonic reflectometry, which to the authors' best knowledge, for the first time enables detailed visualisation of contact patch and pressure distribution of both wheel–rail contact and wheel–endpost contact. Together with FE simulations, specific findings are listed as follows:

- The ultrasonic measurements are in good agreement with FE simulations in terms of both contact areas and contact pressure levels, especially at the most concerning rail edges;
- The ultrasonic measurements can capture more details on contact pressure with surface roughness and irregularities considered;
- Regardless of thickness, the endpost normally sustains contact pressure no more than 100 MPa and either contact area or pressure level does not increase when the normal load goes beyond 30 kN;
- The endpost deforms in a concave manner along the longitudinal direction, and most of the load is supported by the rail edges on two sides which tends to deform into tiny chamfer-like areas at the sharp corners, generating much higher contact pressure than normal wheel tread-rail head contact, making the region more vulnerable to wear and failures;
- Increasing the endpost thickness may enhance the service life of the component individually but will also remarkably increase the pressure level at rail edges, therefore an optimised selection balancing the two concerns is preferable.

This study marks a prelude of our investigation series starting from characterisation of static IRJ contacts as presented in this paper, and it should be admitted that dynamic contacts on operating railway lines are of more practical values. While characterising dynamic contacts through ultrasonic reflectometry is already realised in the authors' previous work [37–40], implementing ultrasonic array on rail is not feasible for the IRJ contact which contains both rail and endpost components. A possible solution can be sought as envisaged in [38] by mounting the sensing elements that rotate synchronously with the travelling train on the inner rim of the wheel. The plan is to use an ultrasonic array with small size lead zirconate titanate (PZT) sensing elements. Each of the sensing element is 2 mm or 1 mm wide in the lateral direction to provide high-resolution scanning. Moreover, a set of calibration tests have been conducted [47] and continuously updated concerning different categories of wheel/rail surface roughness state, e.g. new, worn, sand damaged, etc. In real applications, surface roughness of the monitored region will be measured through profilometre so that which category the monitored area falls into is known, and the corresponding calibration curve will be applied. Upon *in-situ* tests conducted with more ultrasonic measurements, it is expected that the contact behaviours of IRJs under passing trains can be more systematically revealed.

Data availability statement

The data that support the findings of this study are available upon reasonable request from the authors.

Conflict of interest

The author(s) declared no potential conflicts of interest with respect to the research, authorship and/or publication of this article.

Funding

ORCID iD

Yun-Ke Luo ⬤ https://orcid.org/0000-0001-5111-2844

References

[1] Chen Y C and Kuang J H 2002 Contact stress variations near the insulated rail joints *Proc. Inst. Mech. Eng.* F **216** 265–73
[2] Chen Y C 2003 The effect of proximity of a rail end in elastic-plastic contact between a wheel and a rail *Proc. Inst. Mech. Eng.* F **217** 189–201
[3] Chen Y C and Chen L W 2006 Effects of insulated rail joint on the wheel/rail contact stresses under the condition of partial slip *Wear* **260** 1267–73
[4] Sandström J and Ekberg A 2009 Numerical study of the mechanical deterioration of insulated rail joints *Proc. Inst. Mech. Eng.* F **223** 265–73

[5] Mandal N K and Dhanasekar M 2013 Sub-modelling for the ratchetting failure of insulated rail joints *Int. J. Mech. Sci.* **75** 110–22
[6] Mandal N K, Spiryagin M, Berg M and Stichel S 2019 On the railhead material damage of insulated rail joints: is it by ratchetting or alternating plasticity? *Int. J. Fatigue* **128** 105197
[7] Mandal N K, Lewis R and Wen Z 2020 Quantification of sub-surface railhead material damage due to composite endpost materials of insulated rail joints for cyclic wheel loadings *Eng. Fail. Anal.* **113** 104562
[8] Mandal N K, Spiryagin M, Wu Q, Wen Z and Stichel S 2022 FEA of mechanical behaviour of insulated rail joints due to vertical cyclic wheel loadings *Eng. Fail. Anal.* **133** 105966
[9] Yang Z, Boogaard A, Wei Z, Liu J, Dollevoet R and Li Z 2018 Numerical study of wheel-rail impact contact solutions at an insulated rail joint *Int. J. Mech. Sci.* **138** 310–22
[10] Yang Z, Boogaard A, Chen R, Dollevoet R and Li Z 2018 Numerical and experimental study of wheel-rail impact vibration and noise generated at an insulated rail joint *Int. J. Impact Eng.* **113** 29–39
[11] Yang Z, Zhang P and Wang L 2021 Wheel-rail impact at an insulated rail joint in an embedded rail system *Eng. Struct.* **246** 113026
[12] Askarinejad H, Dhanasekar M and Cole C 2013 Assessing the effects of track input on the response of insulated rail joints using field experiments *Proc. Inst. Mech. Eng.* F **227** 176–87
[13] Askarinejad H, Dhanasekar M, Boyd P and Taylor R 2015 Field measurement of wheel—rail impact force at insulated rail joint *Exp. Tech.* **39** 61–69
[14] Beaty P, Temple B, Marshall M B and Lewis R 2016 Experimental modelling of lipping in insulated rail joints and investigation of rail head material improvements *Proc. Inst. Mech. Eng.* F **230** 1375–87
[15] Xiao H, Liu G, Yan D, Zhao Y, Wang J and Wang H 2021 Field test and numerical analysis of insulated rail joints in heavy-haul railway *Constr. Build. Mater.* **298** 123905
[16] Hertz H 1882 Ueber die Berührung fester elastischer Körper *J. Fur Reine Angew. Math.* **1882** 156–71
[17] Kalker J J 1990 *Three-Dimensional Elastic Bodies in Rolling Contact* (Dordrecht: Kluwer)
[18] Luo Y K, Zhou L and Ni Y Q 2022 Towards the understanding of wheel-rail flange squeal: *in-situ* experiment and genuine 3D profile-enhanced transient modelling *Mech. Syst. Signal Process.* **180** 109455
[19] Zhang S L, Koh C G and Kuang K S C 2018 Proposed rail pad sensor for wheel-rail contact force monitoring *Smart Mater. Struct.* **27** 115041
[20] Urda P, Muñoz S, Aceituno J F and Escalona J L 2020 Wheel-rail contact force measurement using strain gauges and distance lasers on a scaled railway vehicle *Mech. Syst. Signal Process.* **138** 106555
[21] Poole W 1987 The measurement of contact area between opaque objects under static and dynamic rolling conditions *Proc. of Contact Mechanics and Wear of the Wheel/rail System* (University of Rhode Island, Waterlooville Press) pp 59–72
[22] Dörner F, Körblein C H and Schindler C H 2014 On the accuracy of the pressure measurement film in Hertzian contact situations similar to wheel-rail contact applications *Wear* **317** 241–5
[23] Brunskill H, Hunter A, Zhou L, Dwyer Joyce R and Lewis R 2020 An evaluation of ultrasonic arrays for the static and dynamic measurement of wheel–rail contact pressure and area *PProc. Inst. Mech. Eng. J.* **234** 1580–93

[24] Shen Y and Cesnik C S 2017 Local interaction simulation approach for efficient modeling of linear and nonlinear ultrasonic guided wave active sensing of complex structures *J. Nondestruct. Eval.* **1** 011008–011008-9

[25] Wang K, Cao W X, Xu L, Yang X B, Su Z Q, Zhang X J and Chen L J 2020 Diffuse ultrasonic wave-based structural health monitoring for railway turnouts *Ultrasonics* **101** 106031

[26] Chen S X, Zhou L, Ni Y Q and Liu X Z 2021 An acoustic-homologous transfer learning approach for acoustic emission–based rail condition evaluation *Struct. Health Monit.* **20** 2161–81

[27] Li D, Wang Y, Yan W J and Ren W X 2021 Acoustic emission wave classification for rail crack monitoring based on synchrosqueezed wavelet transform and multi-branch convolutional neural network *Struct. Health Monit.* **20** 1563–82

[28] Hao Q, Shen Y, Wang Y and Liu J 2021 An adaptive extraction method for rail crack acoustic emission signal under strong wheel-rail rolling noise of high-speed railway *Mech. Syst. Signal Process.* **154** 107546

[29] Loveday P W, Long C S and Ramatlo D A 2020 Ultrasonic guided wave monitoring of an operational rail track *Struct. Health Monit.* **19** 1666–84

[30] Mariani S and Di Scalea F L 2018 Predictions of defect detection performance of air-coupled ultrasonic rail inspection system *Struct. Health Monit.* **17** 684–705

[31] Hu P, Wang H, Tian G, Liu Y, Li X and Spencer B F 2020 Multifunctional flexible sensor array-based damage monitoring for switch rail using passive and active sensing *Smart Mater. Struct.* **29** 095013

[32] Zhou L, Chen S X, Ni Y Q and Choy A W H 2021 EMI-GCN: a hybrid model for real-time monitoring of multiple bolt looseness using electromechanical impedance and graph convolutional networks *Smart Mater. Struct.* **30** 035032

[33] Zhou L, Chen S X, Ni Y Q and Jiang L 2021 Pitch-catch UGW-based multiple damage inference: a heterogeneous graph interpretation *Smart Mater. Struct.* **31** 015005

[34] Huo L, Wang F, Li H and Song G 2017 A fractal contact theory based model for bolted connection looseness monitoring using piezoceramic transducers *Smart Mater. Struct.* **26** 104010

[35] Wang F, Huo L and Song G 2017 A piezoelectric active sensing method for quantitative monitoring of bolt loosening using energy dissipation caused by tangential damping based on the fractal contact theory *Smart Mater. Struct.* **27** 015023

[36] Marshall M B, Lewis R and Dwyer-Joyce R S 2006 Characterisation of contact pressure distribution in bolted joints *Strain* **42** 31–43

[37] Zhou L, Brunskill H and Lewis R 2022 Experimental investigation on ball plate contact using ultrasonic reflectometry: from static to dynamic *Ultrasonics* **124** 106733

[38] Zhou L, Brunskill H P and Lewis R 2019 Real-time non-invasive measurement and monitoring of wheel–rail contact using ultrasonic reflectometry *Struct. Health Monit.* **18** 1953–65

[39] Zhou L, Brunskill H, Pletz M, Daves W, Scheriau S and Lewis R 2019 Real-time measurement of dynamic wheel-rail contacts using ultrasonic reflectometry *J. Tribol.* **141** 6

[40] Zhou L, Marshall M B and Lewis R 2017 Wheel-rail endpost contact characterisation using ultrasound reflectometry *Int. J. Railw. Technol.* **6** 29–49

[41] Kendall K and Tabor D 1971 An ultrasonic study of the area of contact between stationary and sliding surfaces *Proc. R. Soc.* A **323** 321–40

[42] Thomas T R and Sayles R S 1977 Stiffness of machine tool joints: a random-process approach *J. Eng. Ind.* **99** 250–6

[43] Krautkrämer J and Krautkrämer H 1990 *Ultrasonic Testing of Materials* 4th edn (Berlin: Springer)

[44] Taxt T 1997 Comparison of cepstrum-based methods for radial blind deconvolution of ultrasound images *IEEE Trans. Ultrason. Ferroelectr. Freq. Control* **44** 666–74

[45] Taxt T and Strand J 2001 Two-dimensional noise-robust blind deconvolution of ultrasound images *IEEE Trans. Ultrason. Ferroelectr. Freq. Control* **48** 861–6

[46] Pham D H, Basarab A, Zemmoura I, Remenieras J P and Kouamé D 2020 Joint blind deconvolution and robust principal component analysis for blood flow estimation in medical ultrasound imaging *IEEE Trans. Ultrason. Ferroelectr. Freq. Control* **68** 969–78

[47] Marshall M B, Lewis R, Dwyer-Joyce R S, Olofsson U and Björklund S 2004 Ultrasonic characterisation of a wheel/rail contact *30th Leeds-Lyon Symp. on Tribology, Inst Natl Sci Appl, Lyon,* (*FRANCE, September 02–05 2003*) vol 43 pp 151–8

[48] Eadie D T, Santoro M and Powell W 2003 Local control of noise and vibration with KELTRACKTM friction modifier and Protector® trackside application: an integrated solution *J. Sound Vib.* **267** 761–72

[49] Polach O 2005 Creep forces in simulations of traction vehicles running on adhesion limit *Wear* **258** 992–1000